Accurate valence band width of diamond

I. Jiménez, L. J. Terminello, D. G. J. Sutherland, and J. A. Carlisle
Lawrence Livermore National Laboratory, Livermore, California 94550

E. L. Shirley
National Institute of Standards and Technology, Optical Technology Division, Gaithersburg, Maryland 20899

F. J. Himpsel
Department of Physics, University of Wisconsin-Madison, Madison, Wisconsin 53706

An accurate width is determined for the valence band of diamond by imaging photoelectron momentum distributions for a variety of initial- and final-state energies. The experimental result of 23.0 ± 0.2 eV^2 agrees well with first-principles quasiparticle calculations (23.0 and 22.88 eV) and significantly exceeds the local-density-functional width, 21.5 ± 0.2 eV^2. This difference quantifies effects of creating an excited hole state (with associated many-body effects) in a band measurement vs studying ground-state properties treated by local-density-functional calculations. [S0163-1829(97)05136-9]

I. INTRODUCTION

The bandwidth may be considered the single most important parameter characterizing the electronic structure of a solid. The ratio of bandwidth W and Coulomb repulsion U determines how correlated ($U/W>1$) or delocalized ($U/W<1$) an electron system is. Some of the most interesting solids straddle the boundary between localized and delocalized systems, e.g., high-temperature superconductors. Most band calculations available today are based on local-density-functional (DF) theory.[1,2] Even though Kohn-Sham eigenvalues[2] from that theory do not represent the outcome of a photoemission band-mapping experiment, they are remarkably similar to band energies mapped experimentally. Strictly speaking, one should use a formulation addressing the solid's many-body effects on the energy required to create a hole in photoemission. Quasiparticle (QP) calculations of band energies, which use Dyson's equation, include such many-body corrections via the electron self-energy.[3–7]

Angle-resolved photoemission experiments have become accurate enough to see many-body effects on the bandwidth by comparing data with DF and QP calculations. For sodium, a prototype metal, the measured occupied bandwidth is smaller than the DF value but is close to the QP result.[6,8,9] On the other hand, the measured bandwidth in LiF, a prototype insulator, is larger than the DF value, and in agreement with the QP result.[4,10] Between such extremes, one may consider many-body effects on bandwidths in semiconductors. Because their properties are intermediate between those of metals and insulators, it is not clear whether many-body effects should narrow or widen bands. Calculations within the jellium model[6] indicate that metals having an electron density comparable to semiconductors could have DF-like bandwidths, particularly for diamond with $r_s\approx1.3$, whereas true semiconductors also exhibit a wide variety of band gaps and varying degrees of nearly free-electron character, average r_s, and ionicity.

Comparing DF and QP results gives a band widening for semiconductors, just as in wide-gap insulators, but the widening is too small to be confirmed with the available data. The predicted band widening is only 0.05 eV in germanium and 0.08 eV in silicon[4,7] (both systems having $r_s\approx2.0$), i.e., widenings smaller than the typical uncertainty in a valence-band minimum determined by angle-resolved photoemission. Diamond is a better-suited system wherein to observe a widening because of many-body effects, featuring a 1.5 eV widening as predicted by QP calculations.[4,5,7] Diamond is a useful prototype semiconductor because of its low atomic number and large bandwidth, which has made it a long-time favorite for testing band theory. Yet, the two experimental values of the bandwidth of diamond have error bars of ±1 eV and differ by 3.2 eV,[11,12] which is more than twice the predicted widening of 1.5 eV.

To obtain an accurate (valence) bandwidth for diamond, we use a band-mapping method that collects isoenergy photoelectron momentum distributions instead of the usual energy distributions. This approach has undergone extensive experimental and theoretical tests in determining the bandwidth of lithium fluoride.[10] An efficient, imaging photoelectron spectrometer[13] is coupled with a state-of-the-art undulator beam line at the Advanced Light Source (ALS) to permit collecting a large number of data sets. Because it takes only a few seconds to take an image of the photoelectrons emitted into an 84° full cone, we could use photon energies as high as 350 eV, where the photoemission cross section from the valence band is quite low, but photoelectrons behave free-electron-like before leaving the solid. This makes it much easier to locate the origin of the interband transitions in momentum space.

The result of our band mapping is a bandwidth of 23.0 ±0.2 eV, which agrees well with QP results by Hybertsen and Louie[4] (23.0) and by Rohlfing, Kruger, and Pollmann[7] (22.88 eV). The band widening of 1.5 eV (7%) compared to the DF bandwidth (21.67 eV by Hybertsen and Louie, 21.35 eV by Rohlfing, Kruger, and Pollmann) is clearly visible. The origin of this widening might be understood as an in-
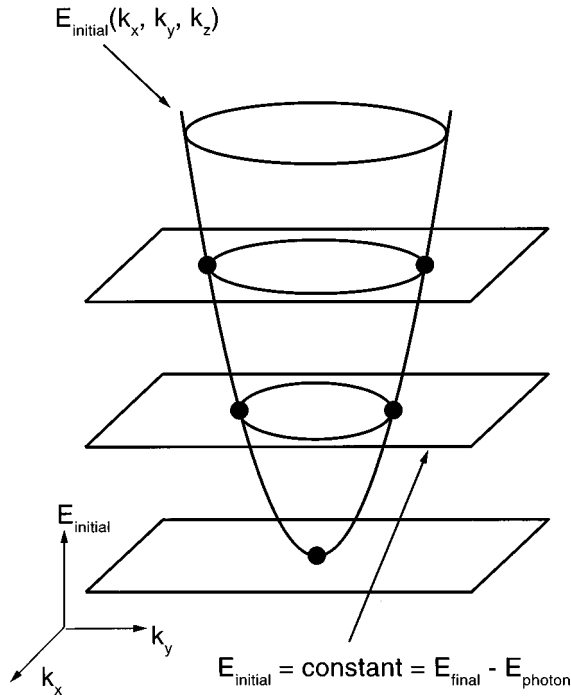
FIG. 1. Schematic of the experiment in $(E, \mathbf{k}^{\parallel})$ space. The planes indicate initial-state isoenergy surfaces, and the paraboloid the band structure near the valence-band minimum. The intersection of a plane and the paraboloid forms a loop that is visible in the experimental image. At the band minimum, the loop shrinks to a point for appropriate k_z. Note that k_z is defined implicitly by the band dispersion of the final state.
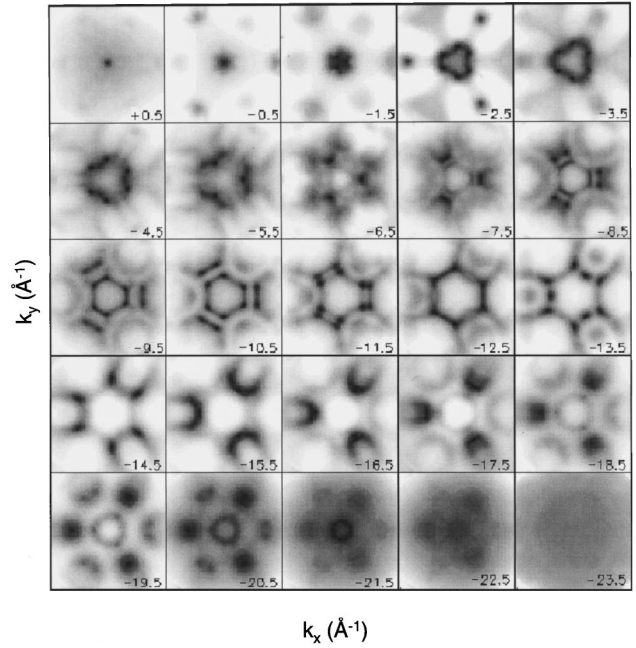

FIG. 2. Images of photoelectron momentum distributions for several initial-state energies across the entire valence band of diamond. The kinetic energy (final-state energy) is kept constant at 142 eV, corresponding to a point near $\Gamma_{(222)}$ (Ref. 16). When the band extrema are approached, the emission pattern shrinks to a point at the center (normal emission). The initial-state energies are given, in eV, relative to the valence-band maximum. Each frame covers $7.6 \, \text{Å}^{-1} \times 7.6 \, \text{Å}^{-1}$.

creasing localization of electron states towards the bottom of the band, together with the fact that energies of such localized states tend to be too high in DF calculations.

II. EXPERIMENT

Our data are images of photoelectron momentum distributions emitted with given kinetic energies. Such images were taken for $\approx 10^2$ combinations of electron and photon energies. The basic idea is outlined in Fig. 1. By selecting some final-state energy, one defines a momentum sphere which intersects many isoenergy surfaces in the band structure describing electron initial states (to use the standard terminology which describes photoemission in an independent-electron picture). Conceivably, the intersection can correspond to closed contours which shrink to a point for initial states at band extrema, and observing such shrinkage gives an accurate bandwidth. The data in Fig. 2 illustrate the method. While isoenergy contours are rather complex within the band, they become simpler near band edges, shrinking to points at the maximum (defined as the energy zero) and minimum (around -23.0 eV).

Before taking a set of images versus initial energy, such as in Fig. 2, the final-state (kinetic) energy of the photoelectrons needs to be adjusted. In so doing, the momentum normal to the surface, k_z, is set to a value equivalent to the Γ point in the bulk Brillouin zone, where the valence-band extrema are located, cf. Fig. 3. [The coordinate system for (k_x, k_y, k_z) is indicated in Fig. 1, whereas the (111) *crystallographic* direction corresponds to the k_z direction.] Then, a

series of images is obtained for several initial-state energies across the valence band by varying photon energy, cf. Figs. 2 and 4.

The imaging electron spectrometer used for this work is an improved version of a display analyzer described previously.[13] It combines an ellipsoidal electron-repelling mirror as low pass with a spherical retarding grid as high pass. Photoelectrons emitted within an 84° full cone around the sample normal are imaged onto a channel plate and read out optically. A new feature is a segmentation of the ellipsoidal mirror into five elements with three slightly different bias voltages, which compensates for the change in angle of incidence along the elliptical direction of the electron mirror. This produces a threefold-higher resolving power or, alternatively, better homogeneity of the band pass across the field of view. The instrument is operated at an undulator beam line at the ALS (5-cm period), where the data-acquisition time is reduced to less than 30 s per image, compared to about 30 min at a second-generation light source. The intensity is normalized to the transmission of the analyzer, as measured from the emission of secondary electrons. The latter are produced at higher photon energy while preserving the analyzer settings. Threefold symmetrization suppresses inhomogeneities and polarization effects, although all features discussed here are clearly visible in the raw data. The normalized images are converted into momentum distributions numerically, using the analyzer geometry and reference data from the sharp Fermi surface of graphite for calibration.

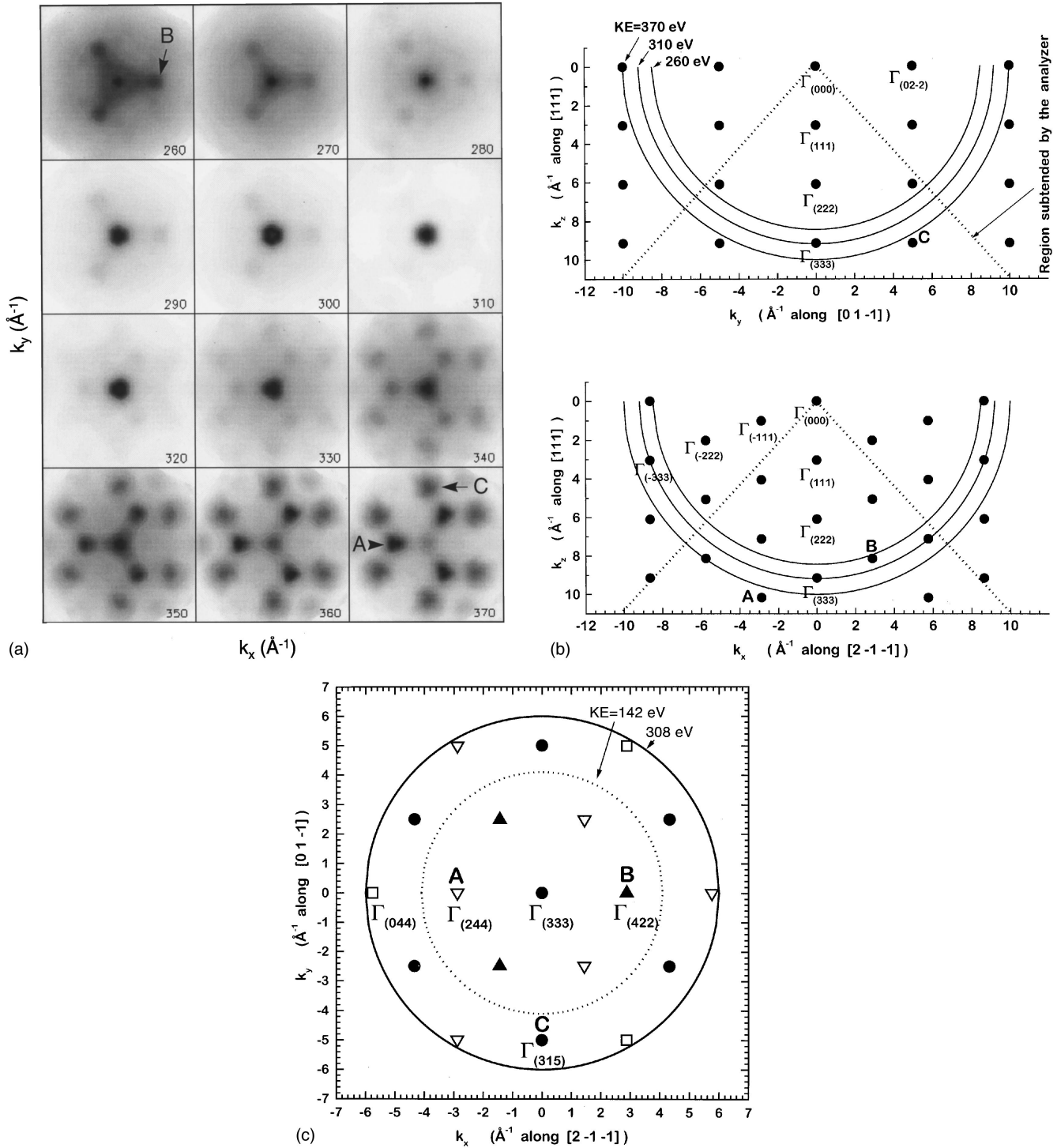A hydrogen-terminated diamond (111)-1×1 surface was prepared from a naturally boron-doped, type-IIb diamond

FIG. 3. (a) Images of (k_x, k_y) photoelectron momentum distributions for hydrogen-terminated diamond (111)-1×1. The initial-state energy is fixed at the valence-band maximum, while the final-state energy is varied, in order to vary the perpendicular momentum k_z. At $\Gamma_{(333)}$, the emission pattern shrinks to a point corresponding to normal emission. This defines the $\Gamma_{(333)}$ point for electrons with final-state kinetic energy of 308 eV. Each frame covers 12 Å^{-1}×12 Å^{-1}. (b) Schematic of transitions in (a) in (k_x, k_z) plane (bottom) and (k_y, k_z) plane (top). Points of type A and B produce the triangular spots surrounding the central spot in (a) when the final-state energy is higher than $\Gamma_{(333)}$ and lower than $\Gamma_{(333)}$, respectively, and points of type C produce the hexagonal pattern at high energies. (c) Schematic of (a) in the (k_x, k_y) plane. The circles represent the reciprocal space monitored by the analyzer (corresponding to a subtended full-cone angle of 84°).

cleavage surface as described earlier.[11] Heating in ultrahigh vacuum to 900 K sharpened the C($1s$) core-level spectrum without destroying the hydrogen termination of broken bonds. The clean 2×1 surface obtained after further heating to 1300 K showed a well-resolved surface component of the

C($1s$) signal and introduced surface states into the valence-band spectra. Such states hamper identification of bulk features and blur angular distributions by introducing extra momentum transfer via the 2×1 surface lattice. The hydrogen-terminated 1×1 surface does not exhibit such surface states
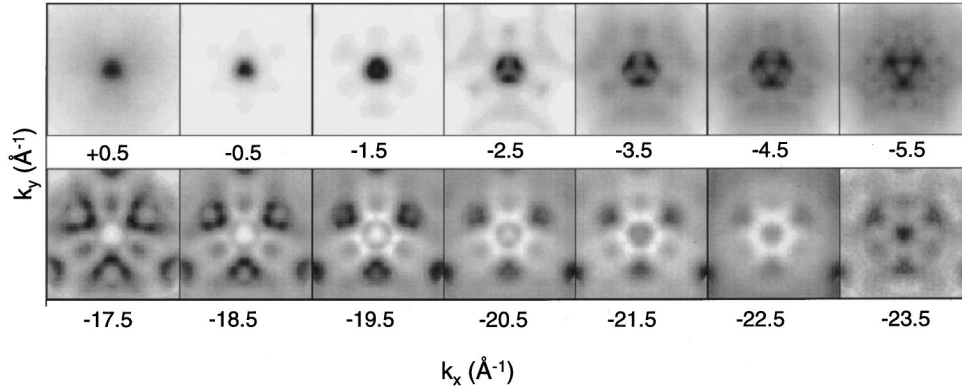
FIG. 4. Images of (k_x, k_y) photoelectron momentum distributions for initial states near valence-band maximum (top row) and minimum (bottom row). The final-state (kinetic) energy is kept constant at 308 eV, corresponding to the $\Gamma_{(333)}$ point. Initial-state energies are given in eV relative to the valence-band maximum. Each frame covers 12 Å^{-1} × 12 Å^{-1}.

at the band edges, as evidenced by photoemission[11] and by band calculations[14] for the isostructural, hydrogen-terminated Si(111)-1×1 surface. Therefore, only the hydrogen-terminated surface was used for determining the bulk bandwidth.

III. EXPERIMENTAL DETERMINATION OF THE BAND WIDTH

Sample momentum distributions are given in Figs. 2, 3(a), and 4, with regions of high electron-emission intensity shown dark, because representation of images as negatives enhances visibility of the weakest features. In Fig. 3(a) the final-state energy of the photoelectrons is varied for fixed initial-state energy, but in Figs. 2 and 4 the initial-state energy is varied for fixed final-state energy. As stated earlier, these are the two main steps of the bandwidth measurements.

In the first step [Fig. 3(a)], the final-state energy is adjusted to ensure that a transition can be observed at the Γ point of the bulk Brillouin zone ($\mathbf{k}=\mathbf{0}$). For the final states, there is a series of Γ points along the (111) sample normal [Fig. 3(b)] corresponding to the (111), (222), (333), etc. reciprocal-lattice vectors (in units of $2\pi/a$ with the lattice constant $a=3.567$ Å). In a free-electron band, these Γ points are reached at energies of 35.5, 142, and 319 eV above the bottom of the band, respectively. In Fig. 3(a), we consider the $\Gamma_{(333)}$ point and determine a (vacuum) kinetic energy of 308 eV for it, implying an inner potential of -11 eV. This is found by taking images at a series of final-state energies while keeping the initial-state energy at the valence-band maximum. Transitions to the $\Gamma_{(333)}$ point are seen as point-like emission at the center of the images in Fig. 3(a). At 308 eV, the intensity of this emission reaches a maximum relative to neighboring Γ points, e.g., the points marked A and B in Figs. 3(a), 3(b), and 3(c). For kinetic energies below the $\Gamma_{(333)}$-point transition (e.g., 260 eV), one observes a triangle of Γ points equivalent to B with a corner on the right-hand side. Above the $\Gamma_{(333)}$ transition, there is similarly a triangle with a corner on the left (e.g., at 370 eV), plus an outer hexagon. As shown in Fig. 3(b) (bottom), the additional triplet spots A and B correspond to Γ points located on (111) planes 1.02 A^{-1} above and below the plane containing $\Gamma_{(333)}$. The outer hexagon of points of type C correspond to

other Γ points located in the (333) plane [Fig. 3(b), top]. An analogous procedure yields a kinetic energy of about 131 eV for the $\Gamma_{(222)}$ point. After determining the kinetic energy for the final-state Γ point, the kinetic energy is fixed in all further images.

In the second step, the initial-state energy is varied to scan across the valence band in constant-final-state mode. Figure 2 shows images that span the entire valence-band with the final-state energy fixed near the $\Gamma_{(222)}$ point. We observe a sharp spot at the center ($\mathbf{k}^{\parallel}=\mathbf{0}$) near the top of the band. For decreasing energy, the central spot opens up into a circle, and the circle splits further because of light- and heavy-hole bands. Near the middle of the valence band, the topology of the momentum distributions becomes rather complex, but it simplifies again near the bottom of the band, which mirrors the behavior at the top, with a circular feature shrinking to a point at the very bottom.

Figure 4 contains images similar to Fig. 2, but with the final state fixed at the $\Gamma_{(333)}$ point instead of near the $\Gamma_{(222)}$ point. They are taken at finer energy intervals to allow an accurate determination of the valence-band extrema. At that energy, the photoemission cross section at the valence-band minimum is larger than near the $\Gamma_{(222)}$ point, making the images in Fig. 4 more suitable for this determination (Figs. 5 and 6). Intensity profiles along the k_y direction in Fig. 4 are displayed in Fig. 5 for states near the valence-band maximum. They are decomposed into Gaussian profiles to better distinguish various valence-band features, which is critical near the band edges, where transitions on either side of the zone center are superposed. The distance between two unresolved peaks can be determined unambiguously by fixing the width of the Gaussians to the sharpest overall width, obtained at the band extrema. A similar analysis is performed for the dispersion near the valence-band minimum (not shown). Plotting the momenta k_y of the features at various initial-state energies, we obtain the energy bands near the maximum and minimum in Fig. 6. Then, by fitting parabolas to the band edges, we obtain accurate values for the valence-band extrema and hence for the valence band width (dashed lines in Fig. 6).

IV. EXPERIMENTAL VS QUASIPARTICLE BANDS

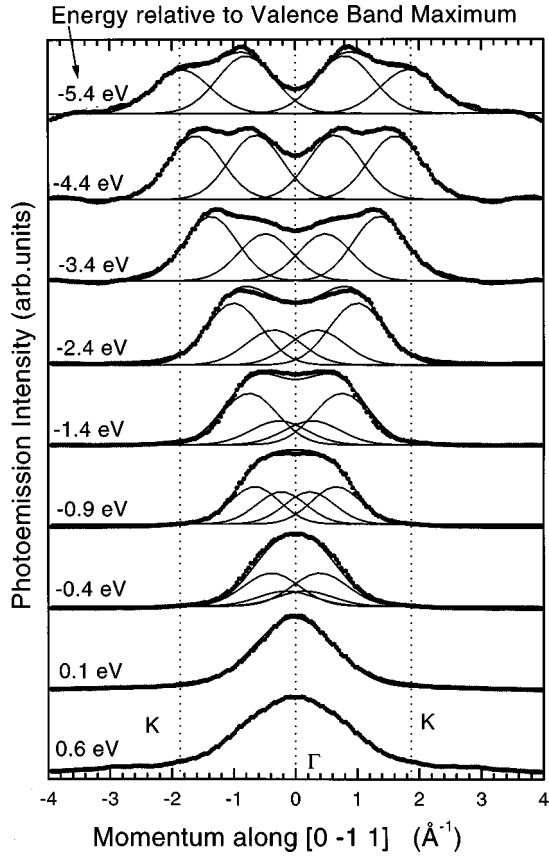The diamond bulk band structure has been extensively studied, and the data may be compared with QP results,

FIG. 5. Set of radial intensity profiles along the y direction in Fig. 4 (vertical). Gaussian fits with constrained width are used to precisely determine momenta where the transitions occur for various photon energies.
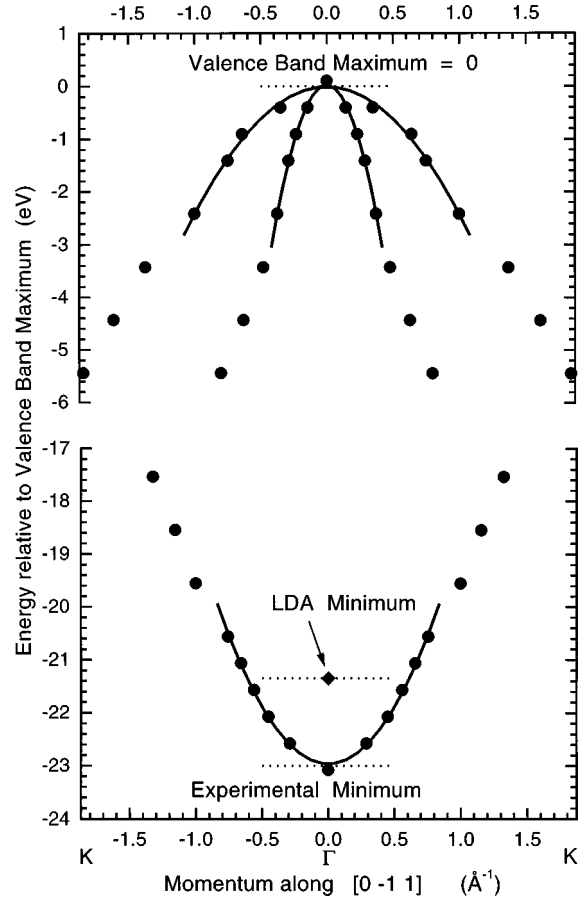

FIG. 6. Interband transitions in an (E,k_y) diagram. A parabolic fit to data near band edges is used to determine the valence-band maximum and minimum. It gives a bandwidth of 23.0 ± 0.2 eV, substantially larger than the density-functional result, 21.5 ± 0.2 eV.

which were given by Hybertsen and Louie,[4] Godby, Schüter, and Sham,[5] and Rohlfing, Kruger, and Pollmann.[7] These results yield a 1.5-eV enhancement in bandwidth compared to DF results. Indeed, QP results for diamond valence bands exhibit a uniform 7% ''stretch'' compared to DF results. This facilitates modeling electron band states readily using suitably amended, convenient DF results, which we did in a fashion greatly accelerated by the choice of an optimal basis set,[15] to treat band dispersion and simulate photoelectron momentum distributions. Regarding further details on the treatment of one-electron band states, the calculations were similar to those in Ref. 15.

In calculated momentum distributions, weightings of C($2s$) and C($2p$) orbitals in initial-state wave functions were determined and used to compute matrix elements for photoexcitation into several nearly degenerate outgoing plane waves, one of which corresponds to the vacuum plane-wave part of the final state. Couplings between such plane waves were computed within the pseudopotential/plane-wave framework which was used, including effects of non-local pseudopotential projectors. We assumed a mean free path of 10 Å, and due preferential weighting of orbitals on the atoms closer to the surface was taken into account. For necessary integration over k_z, results presented include a sampling of 30 k_z values over a 1 Å^{-1} range centered around $\langle k_z \rangle \equiv (K^2 - k_x^2 - k_y^2)^{1/2}$, with $K \approx 6.33$ Å^{-1}. Because we worked within a pseudopotential framework, care was taken to evaluate atomic orbital weights using solid-state,

pseudo wave functions, but plane-wave matrix elements were corrected using known differences between full and pseudo wave functions in atomic core regions. A simpler approximation worked well in graphite and LiF, but more care may be required in diamond, which exhibits stronger admixture of atomic $2s$ and $2p$ states. Calculated momentum distributions for final states near[16] the $\Gamma_{(222)}$ point are encouraging, featuring theoretical counterparts to several experimental features. They are shown in Fig. 7 and correspond to experimental images of Fig. 2.

While QP calculations predict the bandwidth correctly, one may also desire insight into the shortcomings of DF theory regarding predicted bandwidths. In the following, we propose a qualitative argument to explain the differences between DF results and the true band structure. We note opposite trends for wide-gap insulators LiF and the semiconductor diamond vs the nearly free-electron metal, sodium. Rather than formulating a distinction between metallic vs nonmetallic systems, we note that many-body effects on electron states involve exchange, which tends to widen bands, and dynamical correlation, which can widen or narrow bands. For low-density metals, correlation dominates over exchange, leading to an overall band narrowing, whereas exchange dominates at very high densities, even in jellium. Therefore, the many-body effects on such a bandwidth involve two largely canceling parts. The net effect can
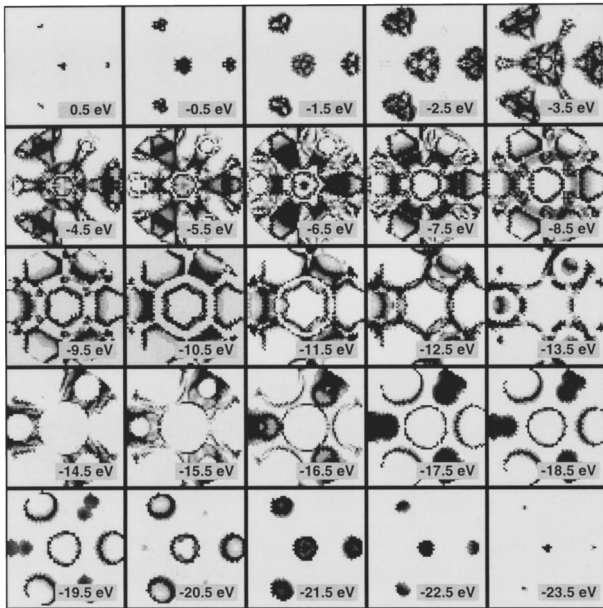
FIG. 7. Simulated photoelectron momentum distributions corresponding to experimental images of Fig. 2. The calculations are based on quasiparticle bands.

be narrowing, widening, or neither.

In diamond and wide-gap insulators, nonjellium character of such systems causes electron states to be more atomic-like, causing DF results to produce an artificial band narrowing. Also, localization can enhance the shortcomings of a DF treatment regarding exchange effects, which cancel spurious "self-interactions" present in many DF treatments, as illustrated most severely for the semicore $3d$ states of zinc[17] and for a localized hydrogen orbital on Si(111)-1×1:H.[14] Also, a DF treatment "envisions" the final-state hole in a photoemission experiment as experiencing the same potential whether it is at the valence-band minimum or maximum (or at the Fermi surface in a metal). However, metallic screening tends to screen a hole at the band minimum more efficiently, an effect not realized in a DF treatment. Therefore, when correlation effects dominate, as they do in sodium, DF results can give too large a bandwidth. For the semimetal graphite, on the other hand, the DF bandwidth is ≈14% smaller than the QP bandwidth.[18]

Recently, a modification to the local-density approximation, the local mass approximation,[19] was designed to obtain the correct bandwidth in simple metals. It also predicts the correct bandwidth for diamond (22.9 eV), where the difference between experiment and local-density theory goes in the opposite direction.

V. CONCLUSIONS

In summary, we demonstrate how an extensive set of photoelectron momentum distributions can be used to determine a bandwidth with unsurpassed accuracy. This result and other successful applications of photoelectron momentum distributions[10,20–22] suggest that viewing photoemission data in two- or three-dimensional momentum space rather than in one-dimensional energy space can be advantageous. For diamond, we obtain a bandwidth of 23.0 ± 0.2 eV, allowing one to judge relative merits of local-density-functional and quasiparticle results. The experimental bandwidth agrees with the quasiparticle result, and it is 7% larger than the local-density-functional result. This also illustrates limitations of ground-state calculations such as local-density-functional theory for determining certain properties of systems, whereas quasiparticle calculations address many-body effects on electron-removal energies probed in photoemission. For diamond and other wide-gap materials, we have also provided a motivation for why local-density-functional theory underestimates the bandwidth, which involves the relatively poor treatment by local-density-functional theory of the more localized states at the valence-band minima.

[1] P. Hohenberg and W. Kohn, Phys. Rev. **136**, B864 (1964).

[2] W. Kohn and L. J. Sham, Phys. Rev. **140**, A1133 (1965).

[3] L. Hedin and S. Lundqvist, in *Solid State Physics: Advances in Research and Applications*, edited by F. Seitz, D. Turnbull, and H. Ehrenreich (Academic, New York, 1969), Vol. 23, p. 1.

[4] M. Hybertsen and S. G. Louie, Phys. Rev. Lett. **55**, 1418 (1985); Phys. Rev. B **34**, 5390 (1986).

[5] R. W. Godby, M. Schlüter, and L. J. Sham, Phys. Rev. Lett. **56**, 2415 (1986); Phys. Rev. B **37**, 10 159 (1988).

[6] J. E. Northrup, M. S. Hybertsen, and S. G. Louie, Phys. Rev. Lett. **59**, 819 (1987); Phys. Rev. B **39**, 8198 (1989); For an alternative interpretation, see G. D. Mahan and B. E. Sernelius, Phys. Rev. Lett. **62**, 2718 (1989).

[7] M. Rohlfing, P. Kruger, and J. Pollmann, Phys. Rev. B **48**, 17 791 (1993).

[8] E. L. Shirley, Phys. Rev. B **54**, 7758 (1996).

[9] E. Jensen and E. W. Plummer, Phys. Rev. Lett. **55**, 1912 (1985); In-Whan Lyo and E. W. Plummer, *ibid.* **60**, 1558 (1988).

[10] F. J. Himpsel, L. J. Terminello, D. A. Lapiano-Smith, E. A. Eklund, and J. J. Barton, Phys. Rev. Lett. **68**, 3611 (1992); E. L. Shirley, L. J. Terminello, J. E. Klepeis, and F. J. Himpsel, Phys. Rev. B **53**, 10 296 (1996).

[11] F. J. Himpsel, J. F. van der Veen, and D. E. Eastman, Phys. Rev. B **22**, 1967 (1980); F. J. Himpsel, D. E. Eastman, P. Heimann, and J. F. van der Veen, *ibid.* **24**, 7270 (1981).

[12] F. R. McFeely, S. P. Kowalczyk, L. Ley, R. G. Cavell, R. A.

Pollak, and D. A. Shirley, Phys. Rev. B **9**, 5268 (1974).

[13] D. E. Eastman, J. J. Donelon, N. C. Hien, and F. J. Himpsel, Nucl. Instrum. Methods **172**, 327 (1980); F. J. Himpsel, Braz. J. Phys. **23**, 31 (1993).

[14] K. Hricovini, R. Günther, P. Thiry, A. Taleb-Ibrahimi, G. Indlekofer, J. E. Bonnet, P. Dumas, Y. Petroff, X. Blase, X. Zhu, S. G. Louie, Y. J. Chabal, and P. A. Thiry, Phys. Rev. Lett. **70**, 1992 (1993).

[15] E. L. Shirley, Phys. Rev. B **54**, 16 464 (1996).

[16] The kinetic energy for $\Gamma_{(222)}$ expected from the inner potential of -11 eV would be 131 eV, not 142 eV. The differences in the images are minor.

[17] F. J. Himpsel, D. E. Eastman, E. E. Koch, and A. R. Williams, Phys. Rev. B **22**, 4604 (1980).

[18] X. Zhu and S. G. Louie (unpublished).

[19] G. E. Engel and W. E. Pickett, Phys. Rev. B **54**, 8420 (1996).

[20] A. Santoni, L. J. Terminello, F. J. Himpsel, and T. Takahashi, Appl. Phys. A **52**, 299 (1991); E. L. Shirley, L. J. Terminello, A. Santoni, and F. J. Himpsel, Phys. Rev. B **51**, 13 614 (1995).

[21] P. Aebi, T. J. Kreutz, J. Osterwalder, R. Fasel, P. Schwaller, and L. Schlapbach, Phys. Rev. Lett. **76**, 1150 (1996); P. Aebi, J. Osterwalder, P. Schwaller, L. Schlapbach, M. Shimoda, T. Mochiku, and K. Kadowaki, *ibid.* **72**, 2757 (1994).

[22] G. J. Mankey, K. Subramanian, R. L. Stockbauer, and R. L. Kurtz, Phys. Rev. Lett. **78**, 1146 (1997).